

Article

# Effects of Alkaline Pre-Etching to Metal Hydride Alloys

Tiejun Meng <sup>1</sup>, Kwo-Hsiung Young <sup>1,2,\*</sup> , Chaolan Hu <sup>1</sup> and Benjamin Reichman <sup>1</sup><sup>1</sup> BASF/Battery Materials–Ovonic, 2983 Waterview Drive, Rochester Hills, MI 48309, USA;

pkumeng@hotmail.com (T.M.); sherry.hu@basf.com (C.H.); Benjamin.reichman@basf.com (B.R.)

<sup>2</sup> Department of Chemical Engineering and Materials Science, Wayne State University, Detroit, MI 48202, USA

\* Correspondence: kwo.young@basf.com; Tel.: +1-248-293-7000

Received: 10 September 2017; Accepted: 29 September 2017; Published: 5 October 2017

**Abstract:** The responses of one AB<sub>5</sub>, two AB<sub>2</sub>, four A<sub>2</sub>B<sub>7</sub>, and one C14-related body-centered-cubic (BCC) metal hydrides to an alkaline-etch (45% KOH at 110 °C for 2 h) were studied by internal resistance, X-ray diffraction, scanning electron microscope, inductively coupled plasma, and AC impedance measurements. Results show that while the etched rare earth-based AB<sub>5</sub> and A<sub>2</sub>B<sub>7</sub> alloys surfaces are covered with hydroxide/oxide (weight gain), the transition metal-based AB<sub>2</sub> and BCC-C14 alloys surfaces are corroded and leach into electrolyte (weight loss). The C14-predominated AB<sub>2</sub>, La-only A<sub>2</sub>B<sub>7</sub>, and Sm-based A<sub>2</sub>B<sub>7</sub> showed the most reduction in the internal resistance with the alkaline-etch process. Etched A<sub>2</sub>B<sub>7</sub> alloys with high La-contents exhibited the lowest internal resistance and are suggested for use in the high-power application of nickel/metal hydride batteries.

**Keywords:** metal hydride alloy; nickel metal hydride battery; alkaline bath; high rate performance; superlattice alloys; surface morphology

## 1. Introduction

Metal hydride (MH) alloy, or hydrogen storage alloy, is a group of intermetallic alloys (IMCs) capable of storing hydrogen in the solid form [1]. One of its key applications is the rechargeable nickel/metal hydride (Ni/MH) battery, which is used widely in consumer electronics, as well as stationary and transportation energy storage areas. A large variety of IMCs have been used/proposed as the active materials in the negative electrode of Ni/MH battery, such as A<sub>2</sub>B [2], AB [3,4], AB<sub>2</sub> [5], AB<sub>3</sub> [6], A<sub>2</sub>B<sub>7</sub> [7], A<sub>5</sub>B<sub>19</sub> [8], AB<sub>5</sub> [9], body-centered-cubic (BCC) solid solution [10], and their combinations [11,12]. These IMCs are composed of mostly transition metals (TM), and some may contain rare-earth (RE) elements. The electrochemical high-rate performances of some of these MH alloys were compared in 2010 and the RE-based AB<sub>5</sub> MH alloy had the best high-rate dischargeability (HRD) performance [13]. The magnetic susceptibilities of these alloys, and a couple new ones, were compared in a 2013 article [14]. With several new MH alloys, especially the recently discovered superlattice A<sub>2</sub>B<sub>7</sub>-based ones with improved electrochemical properties, it is important to update the comparison results.

A few pre-activation processes, such as surface fluorination, alkaline bath, acid etch, mechanical alloying, etc., were proposed to shorten the activation process and improve the electrochemical performance of the MH alloys (see a review in [15]). Among these processes, the alkaline bath is very effective in dissolving the native oxide, so as to form a porous oxide surface with catalytic Ni clusters imbedded [13,16–22] and to increase the surface reactive area [23]. In the past, we have used this technique to prepare the alloy for the study of activated surfaces without going through electrochemical formation cycling [24].

## 2. Experimental Set-Up

MH alloys were prepared by either vacuum induction melting (VIM) or arc melting (AM). Details of the melting process were reported before [25,26]. The main difference between these two preparation methods is the size of ingot. While the former is usually used in large production (1–1000 kg), the latter is mostly used in laboratories (5–200 g) [15]. Some alloys went through annealing either in vacuum or Ar. The obtained ingot was hydrided first, followed by grinding and sifting into a –200 mesh size powder. To make the electrode, the powder was compacted directly onto a 1 cm × 1 cm expanded Ni substrate without any binder or conductive metal powder. The loading of powder per electrode ranged from 70 to 100 mg. The KOH etching (activation) experiment was performed on the electrode assembly in 45 wt % KOH at 110 °C for 2 h. After the etching process, the electrode was pulled out, rinsed by deionized water, dried, and tested. A Suzuki-Shokan multi-channel pressure-concentration-temperature system (PCT, Suzuki Shokan, Tokyo, Japan) was used to measure the MH-hydrogen interaction in gaseous phase. PCT measurements at various temperatures were performed after activation, which consisted of a 2 h thermal cycle between room temperature and 300 °C under 2.5 MPa H<sub>2</sub> pressure. A Varian Liberty 100 inductively coupled plasma optical emission spectrometer (ICP-OES, Agilent Technologies, Santa Clara, CA, USA) was used to study the chemical composition of the solution after etching. A Philips X'Pert Pro X-ray diffractometer (XRD, Philips, Amsterdam, The Netherlands) was used to perform the phase analysis, and a JEOL-JSM6320F scanning electron microscope (SEM, JEOL, Tokyo, Japan) was also used to investigate the phase distribution and composition.

A 30 wt % KOH electrolyte, a Hg/HgO reference electrode, and a sintered Ni(OH)<sub>2</sub>/NiOOH counter electrode were used for the electrochemical testing. The internal resistance measurement was performed in the following steps:

- (1) Charge at 0.1 C and discharge at 0.1 C (to -0.7 V vs. Hg/HgO). Record discharge capacity;
- (2) Charge at 0.1 C, discharge 0.1 C to 80% state-of-charge (SOC);
- (3) Conduct internal resistance test at 80% SOC (1st internal resistance test):
  - a. Put in open circuit for 10 min;
  - b. Discharge at 0.5 C for 10 s;
  - c. Charge at 0.5 C for 10 s;
  - d. Put in open circuit for 10 min;
  - e. Discharge at 2 C for 10 s;
  - f. Charge at 2 C for 10 s;
  - g. Put in open circuit for 10 min;
  - h. Calculate internal resistance.
- (4) Charge at 0.1 C back from 80% SOC to 100% SOC;
- (5) Conduct 4 more capacity tests at 0.2 C charge rate and 0.1 C discharge rate. Record discharge capacities;
- (6) Repeat step 3 (2nd internal resistance test);
- (7) Repeat step 4;
- (8) Conduct rate test:
  - a. Charge at 0.2 C, discharge at 0.1 C;
  - b. Charge at 0.2 C, discharge at 0.2 C;
  - c. Charge at 0.2 C, discharge at 0.5 C;
  - d. Charge at 0.2 C, discharge at 1 C;
  - e. Charge at 0.2 C, discharge at 2 C;
  - f. Charge at 0.2 C, discharge at 3 C;

- g. Charge at 0.2 C, discharge at 5 C.
- (9) Repeat step 3 (3rd internal resistance test).

A Solartron 1250 Frequency Response Analyzer (Solartron Analytical, Leicester, UK) with a sine wave amplitude of 10 mV and a frequency range of 0.5 mHz to 10 kHz was used for the alternative current (AC) impedance measurements.

### 3. Results and Discussions

#### 3.1. Alloys Selection

Eight MH alloys (A–H) were selected for this study. The composition and preparation method of each alloy are summarized in Table 1. Details in microstructures of these alloys can be found in the cited reference at the last column in Table 1. A is the most commonly used RE-based AB<sub>5</sub> alloy in the Ni/MH battery. B and C are TM-based AB<sub>2</sub> alloys with dominating C14 and C15 structures, respectively. D is a Laves-phase related BCC solid solution MH alloy composed of a main BCC phase and C14 and TiNi secondary phases, and shows a high capacity at a moderate rate that is suitable for electric vehicle application [12]. Alloys E–H are RE-and Mg-containing A<sub>2</sub>B<sub>7</sub>-based superlattice alloys used mainly in the high-performance consumer Ni/MH batteries [7,27,28]. PCT isotherms measured at 30 °C and room temperature half-cell discharge capacities in the first 10 electrochemical cycles for eight alloys in this study are compared in Figures 1 and 2, respectively. The capacities of these alloys are summarized in Table 1. The BCC-C14 alloy (D) has the highest hydrogen-storage capacity whereas C14 AB<sub>2</sub> alloys (B), and superlattice alloys (E, G, and H) are next, followed by the standard AB<sub>5</sub> alloy (A). The half-cell discharge capacity of C15 AB<sub>2</sub> alloy (C) is the lowest due to its relatively high hydrogen equilibrium pressure, which makes it difficult to charge into higher state-of-charge in the open-air environment. Alloy F has the lowest discharge capacity in the superlattice alloy family (E–H) because of its high Sm-content. From Figure 2, the ease of activation in order is E, F, G > C, H > A > D, B. In general, Mg-containing superlattice alloys are easier to activate, and alloys without La (B, D) take more cycles to reach their maximum capacities. The addition of rare elements to a TM-based MH alloy to improve the activation behavior is a well-known recipe for the preparation of electrochemical applications [29–36].

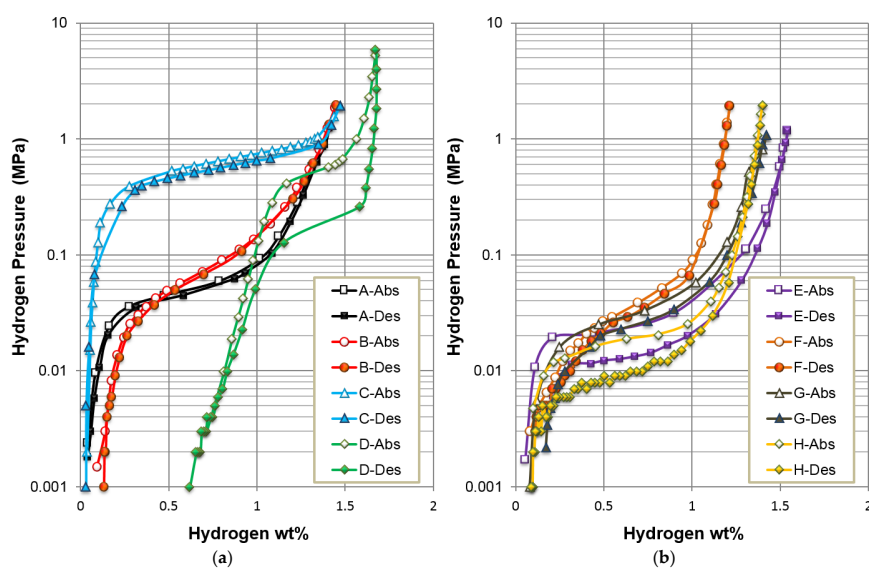


**Figure 1.** Pressure-concentration-temperature system (PCT) isotherms measured at 30 °C for as-is alloys (a) A–D and (b) E–H. Open and solid symbols represent the absorption and desorption curves, respectively.

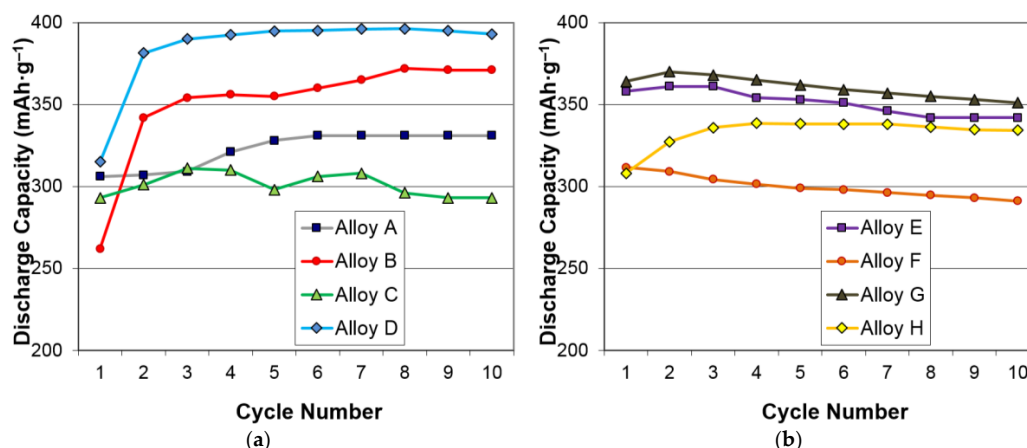


Figure 2. Electrochemical full-capacity activation behavior for as-is alloys (a) A–D and (b) E–H.

Table 1. Preparation and properties of alloys used in this study. Low-rate discharge capacity and saturated magnetic susceptibility ( $M_s$ ) are in the units of  $\text{mAh}\cdot\text{g}^{-1}$  and  $\text{emu}\cdot\text{g}^{-1}$ , respectively. HRDs are the ratio of capacities between 50 and  $4\text{ mA}\cdot\text{g}^{-1}$  for B–D and capacities between 100 and  $8\text{ mA}\cdot\text{g}^{-1}$  for all other alloys.

Alloys	System	Composition	Melting	Annealing	Capacity	HRD	$M_s$	Reference
A	AB <sub>5</sub>	La <sub>10.5</sub> Ce <sub>4.3</sub> Pr <sub>0.5</sub> Nd <sub>1.4</sub> Ni <sub>60</sub> Co <sub>12.7</sub> Mn <sub>5.9</sub> Al <sub>4.7</sub>	VIM	In vacuum	331	0.99	0.43	A in [13]
B	AB <sub>2</sub> -C14	Zr <sub>21.5</sub> Ti <sub>12</sub> V <sub>310</sub> Cr <sub>7.5</sub> Mn <sub>8.1</sub> Co <sub>8</sub> Ni <sub>32.2</sub> Sn <sub>0.3</sub> Al <sub>0.4</sub>	VIM	None	354	0.90	0.04	Mo0 in [37]
C	AB <sub>2</sub> -C15	Zr <sub>25</sub> Ti <sub>6.5</sub> V <sub>3.9</sub> Mn <sub>22.2</sub> Fe <sub>3.8</sub> Ni <sub>38</sub> Sn <sub>0.3</sub> La <sub>0.3</sub>	AM	None	307	0.99	0.04	C15 in [38]
D	BCC-C14	Zr <sub>2.1</sub> Ti <sub>15.6</sub> V <sub>44</sub> Cr <sub>11.2</sub> Mn <sub>6.9</sub> Co <sub>1.4</sub> Ni <sub>18.5</sub> Al <sub>0.3</sub>	VIM	None	397	0.95	0.39	P17 in [39]
E	A <sub>2</sub> B <sub>7</sub>	La <sub>16.3</sub> Mg <sub>7</sub> Ni <sub>65.1</sub> Co <sub>11.6</sub>	VIM	In Ar	361	0.98	0.37	C in [13]
F	A <sub>2</sub> B <sub>7</sub>	La <sub>6</sub> Sm <sub>13.8</sub> Mg <sub>3</sub> Ni <sub>73.8</sub> Al <sub>3.4</sub>	VIM	In Ar	320	0.99	0.60	A3 in [40]
G	A <sub>2</sub> B <sub>7</sub>	La <sub>11.3</sub> Pr <sub>1.7</sub> Nd <sub>5.1</sub> Mg <sub>4.5</sub> Ni <sub>63.6</sub> Co <sub>13.6</sub> Zr <sub>0.2</sub>	VIM	In Ar	370	0.98	1.19	B in [41]
H	A <sub>2</sub> B <sub>7</sub>	La <sub>3.9</sub> Pr <sub>7.7</sub> Nd <sub>7.7</sub> Mg <sub>3.9</sub> Ni <sub>68.1</sub> Co <sub>4.7</sub> Al <sub>4</sub>	VIM	In Ar	354	0.94	0.62	C3 in [42]

### 3.2. Electrochemical Results

Four electrodes from each alloy went through half-cell electrochemical testing. Examples of capacities measured at different rates and three internal resistances ( $R$ ) from alloy A (as-is), alloy B (as-is and etched), and alloy E (as-is and etched) are plotted in Figures 3 and 4. The voltage dropped very quickly with the increase in the discharge current, which resulted in a significant decrease in measured capacity. The etched C14 AB<sub>2</sub> alloy (B) shows the highest discharge capacity, up to a 2 C rate. In the comparison of  $R$ , the etched E shows the lowest resistance, and, in general, the HRD capability is in the order of A<sub>2</sub>B<sub>7</sub> (E) > AB<sub>5</sub> (A) > AB<sub>2</sub> (B) regardless of being etched. This finding is consistent with our previous reports [40,43].

The electrochemical testing results are summarized in Table 2. The reported capacity and internal resistance are highest when obtained with a 0.1 C discharge rate and the lowest value in the three measurements, respectively. The specific power ( $P$ ) was estimated by using formula:

$$P = 2(0.45 - V_{oc})^2/9R \quad (1)$$

where 0.45 and  $V_{oc}$  are the voltage of Ni(OH)<sub>2</sub>/NiOOH electrode and the open-circuit voltage of the tested alloy electrode vs. Hg/HgO reference electrode, respectively. The estimated specific power is

inversely proportional to the measured internal resistance as shown in Figure 5. From Table 2, it is obvious that KOH-etching (activation) is very effective to reduce the internal resistance in C15 AB<sub>2</sub> (C, -25%) and Sm-based A<sub>2</sub>B<sub>7</sub> (F, -19%) alloys. The reduction in the internal resistance is less significant in La-based A<sub>2</sub>B<sub>7</sub> (E, -12%), C14 AB<sub>2</sub> (B, -9%) and Mm-based Al-free A<sub>2</sub>B<sub>7</sub> (G, -8%) alloys. Etching in KOH (activation) even increases the internal resistance of AB<sub>5</sub> (A, +36%) and BCC-C14 (D, +30%) alloys by large percentages. Three A<sub>2</sub>B<sub>7</sub> alloys (E, F, and G) show lower *R* than that of the standard AB<sub>5</sub> (A) after KOH-etching. The as-prepared (no etch) E and G show even lower *R* than that from A and have been used in the high-power design of Ni/MH batteries [41,44]. Overall, G shows the lowest *R* and the highest estimated specific power of 390 W·kg<sup>-1</sup>, which is considerably higher than that from the standard A (317 W·kg<sup>-1</sup>).

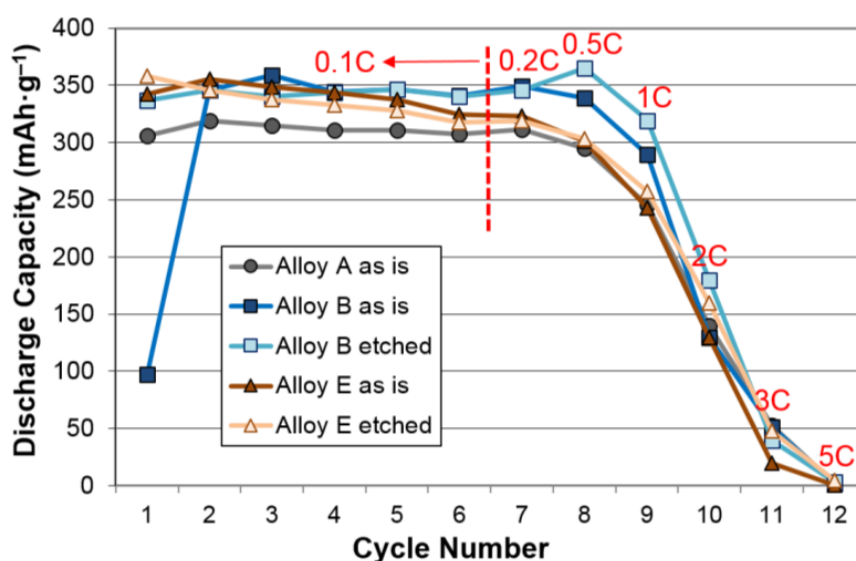


**Figure 3.** Examples of half-cell discharge capacities measured with 0.1 C (cycle 1–6), 0.2 C (cycle 7), 0.5 C (cycle 8), 1 C (cycle 9), 2 C (cycle 10), 3 C (cycle 11), and 5 C (cycle 12) rates from A (as-in only), B (both as-is and etched) and E (both as-is and etched).

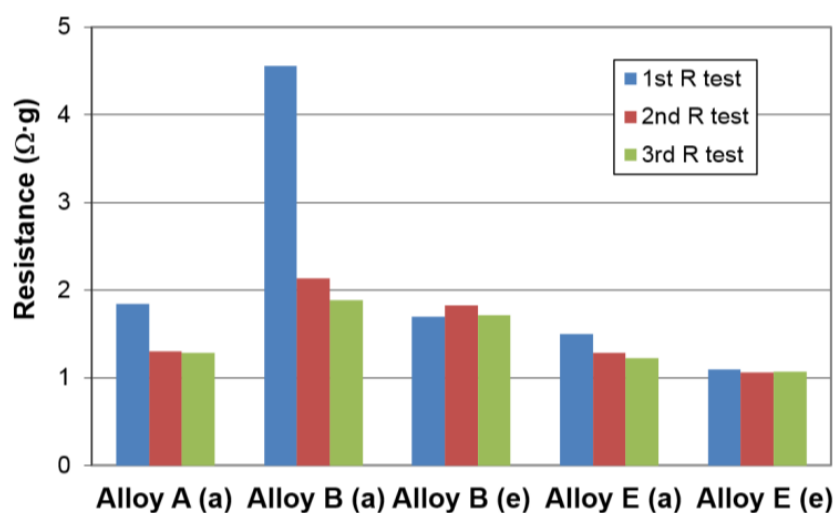


**Figure 4.** Examples of three internal resistance results from A (as-is only), B (both as-is and etched), and E (both as-is and etched). (a) and (e) in parentheses represent for as-is and etched.

**Table 2.** Electrochemical discharge capacity measured at 50 mA·g<sup>-1</sup>, surface charge-transfer resistance (R) from AC impedance measurement, and specific power density.

Alloys	Treatment	Capacity (mAh·g <sup>-1</sup> )	Resistance (Ω·g)	Specific Power (W·kg <sup>-1</sup> )
A	None	321	1.28	317
	KOH-etch	321	1.74	238
B	None	360	1.88*	228*
	KOH-etch	352	1.71*	261*
C	None	290	2.25*	192*
	KOH-etch	291	1.68*	256*
D	None	390	1.80	235
	KOH-etch	349	2.34	181
E	None	356	1.22*	334*
	KOH-etch	358	1.07*	388*
F	None	300	1.42*	287*
	KOH-etch	304	1.15*	355*
G	None	353	1.13*	347*
	KOH-etch	353	1.04*	390*
H	None	345	1.86	218
	KOH-etch	320	2.04	202

Note: \* The reduced R from the KOH-etch treatment.

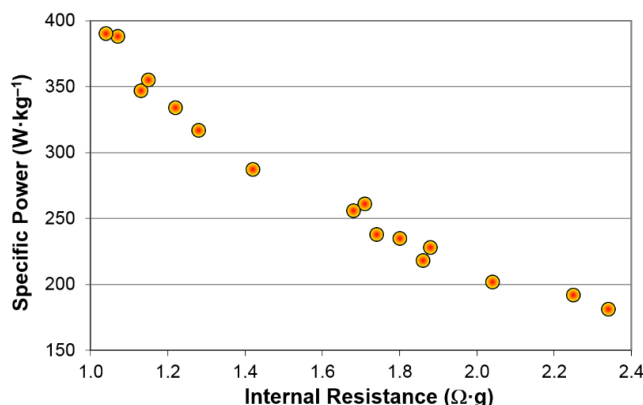


**Figure 5.** Plot of the calculated specific power vs. internal resistance for as-is and etched A–H.

The superiority of E vs. A in the high-rate performance has been verified by room-temperature AC impedance measured at different frequencies as shown in Figure 6. The radius of the semi-circle represents the surface charge-transfer resistance and shows the trend of as-is A > as-is E > etched E, which is in total agreement with the internal resistance measurement.

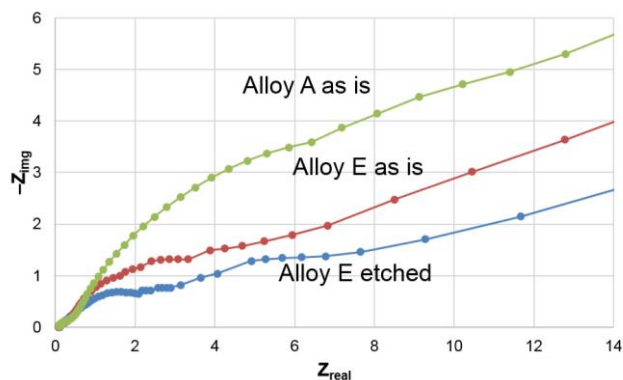


**Figure 6.** Cole-Cole plots obtained from room temperature alternative current (AC) impedance measurements of A (as-is only) and E (both as-is and etched).

The HRD capability of MH alloy was associated with the metallic nickel clusters embedded in its surface oxide after activation [45,46]. The saturated magnetic susceptibility ( $M_S$ ) obtained from the magnetic susceptibility measurement shows clear correlation to the HRD of a series of  $A_2B_7$  MH alloys [13]. However, we also reported that some MH alloys with HRD were more related to the structure of the metal/oxide interface [47,48]. Therefore, it is interesting to compare the internal resistance of the etched alloy with the  $M_S$  values reported in the literature (Table 1). The resulting plot is shown in Figure 7 (red dots) and does not reveal any clear correlation. The difference in  $R$  before and after etching is also plotted in the same figure (triangles) and no clear trend can be seen. We conclude that an  $M_S$  estimation of surface catalytic ability can be used only in the comparison of a series of MH alloys with a similar composition/structure and cannot be elaborated freely among various alloy systems.

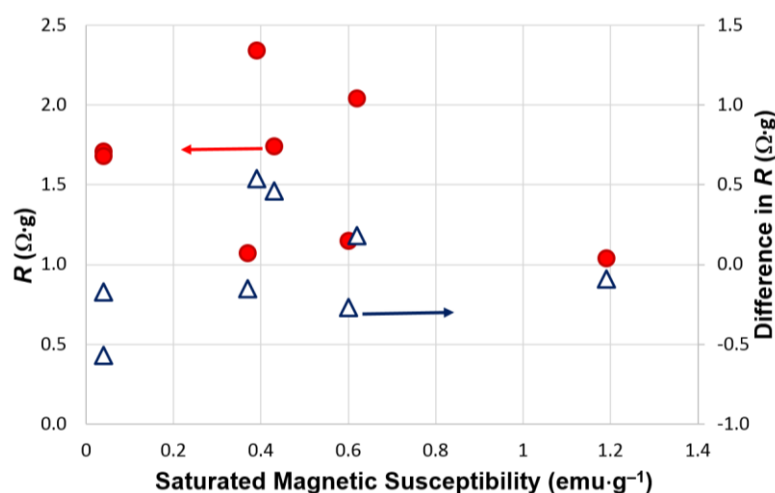


**Figure 7.** Plots of the internal resistance ( $R$  measured from the annealed alloys and the difference in  $R$  before and after annealing (triangle) vs. the saturated magnetic susceptibility ( $M_S$ ) (red dots)).

### 3.3. Microanalysis of the Activated Surface

SEM micrographs taken from the surfaces of etched alloys are shown in Figure 8. While the surfaces of RE-based  $AB_5$  (A) and  $A_2B_7$  (E–H) alloys are covered with  $RE(OH)_3$  needles, those from TM-based  $AB_2$  (B and C) and BCC-C14 (D) are modified by patches of  $ZrO_2$ . Needles from  $La(OH)_3$  are smaller compared to hydroxides from other RE elements [24]. The microstructures of RE- and TM-based MH alloys were studied by transmission electron microscope before and can be summarized as a 50 nm buffer oxide (amorphous) and a 100 nm surface oxide with Ni-inclusion with  $RE(OH)_3$  needles on top in the former and a 100 nm buffer oxide layer and a 200 nm surface oxide with Ni-inclusion with patches of  $ZrO_2$  on top in the latter [24]. While the RE in  $AB_5$  and  $A_2B_7$  alloys formed an impeccable passive surface oxide when reacting with hot KOH, the TM just leaches out into electrolyte. The weight comparison of three B ( $AB_2$ ) and three E ( $A_2B_7$ ) electrodes before and after KOH-etching (dried in vacuum over for 24 h) were conducted and results are listed in Table 3 and plotted in Figure 9. The average weight loss (gain) for B and E (MH powder only) are  $-2.2\%$  and  $+1.0\%$ . The leached-out species were further analyzed by examining the composition of the alkaline solution after the etching experiment with ICP and results are summarized in Table 4. In the solutions with RE-based alloys, only Al (A, F, and H) and a very small amount of Mg (E, F, and G) are detected. In the TM-based alloys (B–D), larger concentrations of Ti, V, and Zr are found. The Ni-concentrations in the solutions from TM-based alloys are much higher than those from the RE-based one, while the former have smaller Ni-content in their compositions. This is additional evidence showing that when the TM-based alloys were attacked by hot KOH they went through a preferential leach-out and the RE-based alloys formed a passive hydroxide layer under the same situation.

To confirm the results from SEM and ICP analysis, XRD was performed, and the resulting patterns obtained before and after KOH-etch for each alloy in this study are plotted in Figure 10. All RE-based MH alloys (A, E–H) show peaks of  $\text{RE}(\text{OH})_3$  after etching. Only etched B shows  $\text{ZrO}_2$  phase, and both  $\text{AB}_2$  alloys (B and C) contain metallic Ni as a product of corrosion after etching. D exhibited a small portion of partially hydride ( $\alpha$ -phase) formed by storing the hydrogen generated from the high level of oxidation of TM (mainly V [11]). The metal-hydrogen bond of the product from the initial hydrogenation is very strong, as seen from the large portion of low-pressure irreversible hydrogen storage in D (PCT in Figure 1). The XRD analysis results indicate that the leaching-out (corrosion) of the alloy surface by hot KOH is in the order of  $\text{D} > \text{C} > \text{B} > \text{the rest}$ .

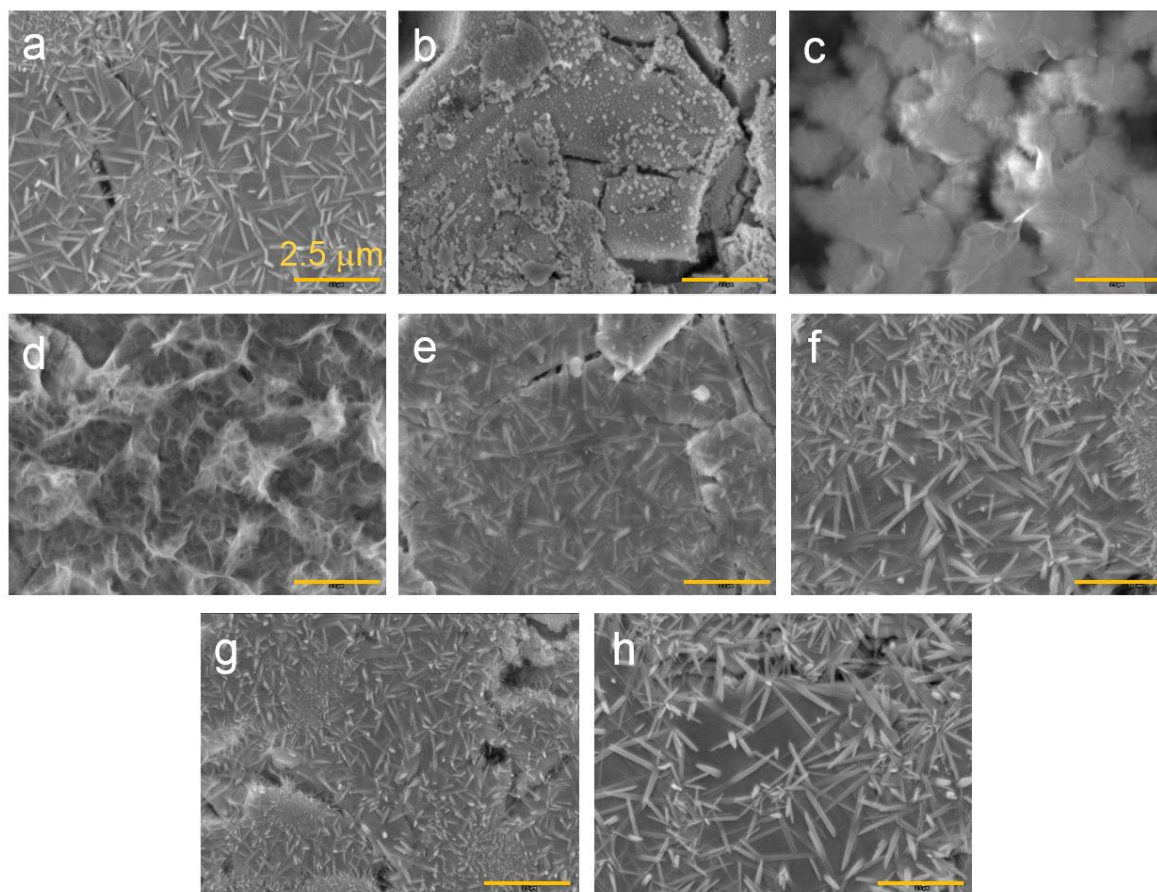


**Figure 8.** Scanning electron microscopy (SEM) micrographs from the etched alloys (a) A, (b) B, (c) C, (d) D, (e) E, (f) F, (g) G and (h) H. The bar at the lower right corner in each micrograph represents 2.5  $\mu\text{m}$ .

**Table 3.** Measurement of weight change before and after KOH-etch for A and B. All numbers are in mg.

Sample #	Substrate Weight	Electrode Weight Before	Electrode Weight After	Weight Difference
B 1	192.8	262.3	260.8	−1.5
B 2	182.7	257.4	255.7	−1.7
B 3	178.4	252.0	250.5	−1.5
E 1	199.5	279.6	280.3	0.7
E 2	181.3	278.7	279.8	1.1
E 3	186.4	289.0	290.1	1.1

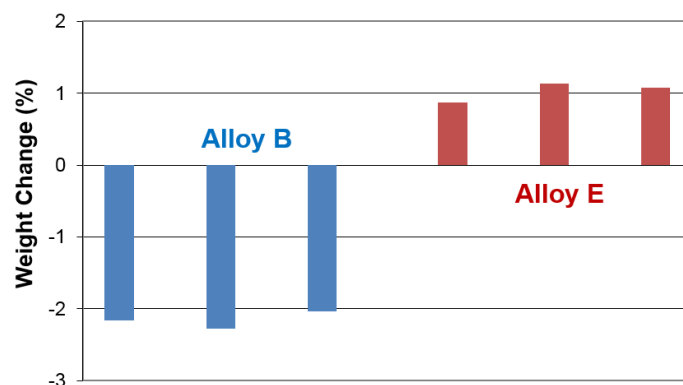


**Figure 9.** Weight changes after KOH-etching for three electrodes from B (left) and three from E (right).

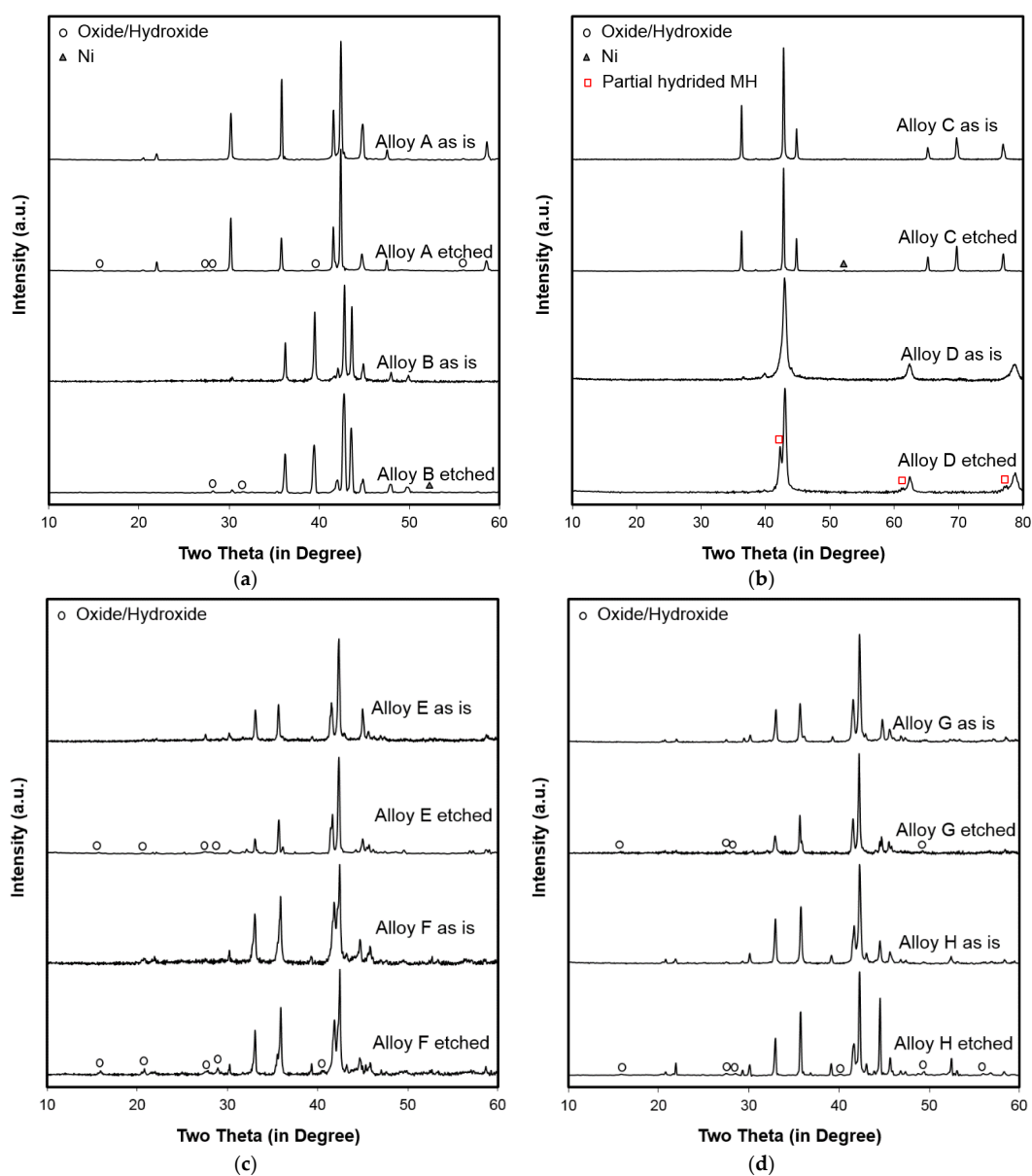


**Figure 10.** X-ray diffractometer (XRD) patterns using Cu- $K_{\alpha}$  as the radiation source for alloys (a) A, B, (b) C, D, (c) E, F and (d) G, H before and after KOH-etching.

**Table 4.** ICP results (in unit of ppm) from the solutions after etching experiment. N.D. and LLD denote non-detectable (below LLD) and lowest limit of detection, respectively.

Alloy	A	B	C	D	E	F	G	H	LLD
Al	58	1.6	N.D.	29	N.D.	78	N.D.	20	0.012
Co	N.D.	0.1	N.D.	1.0	N.D.	N.D.	1.2	N.D.	0.004
Cr	N.D.	4.3	N.D.	48	N.D.	N.D.	N.D.	N.D.	0.054
Fe	N.D.	N.D.	1.0	N.D.	N.D.	N.D.	N.D.	N.D.	0.002
Mg	N.D.	N.D.	N.D.	N.D.	0.05	0.3	0.5	N.D.	0.001
Mn	N.D.	2.0	0.1	8.0	N.D.	N.D.	N.D.	N.D.	0.001
Ni	N.D.	6.0	0.3	5.0	N.D.	N.D.	N.D.	N.D.	0.001
Ti	N.D.	150	7	416	N.D.	N.D.	N.D.	N.D.	0.004
V	N.D.	125	92	988	N.D.	N.D.	N.D.	N.D.	0.013
Zr	N.D.	495	518	309	N.D.	N.D.	N.D.	N.D.	0.002

#### 4. Conclusions

Combining the electrochemical testing results and microstructure analysis, we have the following findings: The improvement in the high-rate capability (reduction in  $R$ ) by KOH-etch is the most prominent in C15 AB<sub>2</sub> (C) with a small La-content, followed by two A<sub>2</sub>B<sub>7</sub> alloys (E and F) with Mg, and then C14 AB<sub>2</sub> (A) and an A<sub>2</sub>B<sub>7</sub> with Mg and no Al (G). The KOH-etch deteriorates the high-rate performance (increase in  $R$ ) in the standard Mg-free AB<sub>5</sub> (A) and V-rich BCC-C14 (D) alloys, whereas Mg-content in A<sub>2</sub>B<sub>7</sub> MH alloys responds well with the KOH-etch and La also helps the decrease in surface charge-transfer resistance by etching. BCC phase in a multiple phase alloy is more robust against the KOH corrosion [49] and is inert in the electrochemical environment [50–52]. Etching at a high temperature will increase the density of BCC phase on the surface and impede the electrochemical reaction, which explains the severe degradation in high-power performance of alloy D after KOH-etch.

**Acknowledgments:** The authors would like to thank the following individuals from BASF-Ovonic for their help: Taihei Ouchi, Jean Nei, Shuan Chang, Su Cronogue, Baoquan Huang, William Mays, Diana F. Wong, David Pawlik, Allen Chan, and Ryan J. Blankenship.

**Author Contributions:** Tiejun Meng performed the experiment and analyzed results. Kwo-Hsiung Young contributed to data analysis and manuscript preparation. Chaolan Hu and Benjamin Reichman provided the KOH-etching recipe and helped in AC impedance measurement and data interpretation.

**Conflicts of Interest:** The authors declare no conflict of interest.

#### Abbreviations

The following abbreviations are used in this manuscript:

MH	Metal hydride
IMC	Intermetallic compound
Ni/MH	Nickel/metal hydride
BCC	Body-centered-cubic
TM	Transition metal
RE	Rare earth
HRD	High-rate dischargeability
VIM	Vacuum induction melting
AM	Arc melting
PCT	Pressure–concentration–temperature
ICP-OES	Inductively coupled plasma-optical emission spectrometer
XRD	X-ray diffractometer
SEM	Scanning electron microscope
SOC	State of charge

$M_S$	Saturated magnetic susceptibility
AC	Alternative current
$R$	Internal resistance
$P$	Specific power
$V_{oc}$	Open-circuit voltage

## References

- Young, K. Metal Hydride. In *Elsevier Reference Module in Chemistry, Molecular Sciences and Chemical Engineering*; Reedijk, J., Ed.; Elsevier: Waltham, MA, USA, 2013.
- Goo, N.H.; Woo, J.H.; Lee, K.S. Mechanism of Rapid Degradation of Nanostructured  $Mg_2Ni$  Hydrogen Storage Alloy Electrode Synthesized by Mechanical Alloying and the Effect of Mechanically Coating with Nickel. *J. Alloys Compd.* **1999**, *288*, 286–293. [[CrossRef](#)]
- Zhang, Q.A.; Lei, Y.Q.; Wang, C.S.; Wang, F.S.; Wang, Q.D. Structure of the Secondary Phase and Its Effects on Hydrogen-storage Properties in a  $Ti_{0.7}Zr_{0.2}V_{0.1}Ni$  Alloy. *J. Power Sour.* **1998**, *75*, 288–291. [[CrossRef](#)]
- Nei, J.; Young, K. Gaseous Phase and Electrochemical Hydrogen Storage Properties of  $Ti_{50}Zr_1Ni_{44}X_5$  ( $X = Ni, Cr, Mn, Fe, Co, \text{ or } Cu$ ) for Nickel Metal hydride Battery Applications. *Batteries* **2016**, *2*, 24. [[CrossRef](#)]
- Züttel, A.; Meli, F.; Schlapbach, L. Electrochemical and Surface Properties of  $Zr(V_xNi_{1-x})_2$  Alloys as Hydrogen-absorbing Electrodes in Alkaline Electrolyte. *J. Alloys Compd.* **1994**, *203*, 235–241.
- Liao, B.; Lei, Y.Q.; Chen, L.X.; Lu, G.L.; Pan, H.G.; Wang, Q.D. A Study on the Structure and Electrochemical Properties of  $La_2Mg(Ni_{0.95}M_{0.05})_9$  ( $M = Co, Mn, Fe, Al, Cu, Sn$ ) Hydrogen Storage Electrode Alloys. *J. Alloys Compd.* **2004**, *376*, 186–195. [[CrossRef](#)]
- Yasuoka, S.; Magari, Y.; Murata, T.; Tanaka, T.; Ishida, J.; Nakamura, H.; Nohma, T.; Kihara, M.; Baba, Y.; Teraoka, H. Development of High-capacity Nickel-metal Hydride Batteries Using Superlattice Hydrogen-Absorbing Alloys. *J. Power Sour.* **2006**, *156*, 662–666. [[CrossRef](#)]
- Zhao, Y.; Zhang, L.; Ding, Y.; Cao, J.; Jia, Z.; Ma, C.; Li, Y.; Han, S. Comparative Study on the Capacity Degradation Behavior of  $Pr_5Co_{19}$ -type Single-phase  $Pr_4MgNi_{19}$  and  $La_4MgNi_{19}$  Alloys. *J. Alloys Compd.* **2017**, *694*, 1089–1097. [[CrossRef](#)]
- Willems, J.J.G.; Buschow, K.H.J. From Permanent Magnets to Rechargeable Hydride Electrodes. *J. Less Common Met.* **1987**, *129*, 13–30. [[CrossRef](#)]
- Young, K.; Ouchi, T.; Huang, B.; Nei, J. Structure, Hydrogen Storage, and Electrochemical Properties of Body-centered-cubic  $Ti_{40}V_{30}Cr_{15}Mn_{13}X_2$  alloys ( $X = B, Si, Mn, Ni, Zr, Nb, Mo, \text{ and } La$ ). *Batteries* **2015**, *1*, 74–90. [[CrossRef](#)]
- Young, K.; Nei, J.; Wong, D.F.; Wang, L. Structural, Hydrogen Storage, and Electrochemical Properties of Laves Phase-related Body-centered-cubic Solid Solution Metal Hydride Alloys. *Int. J. Hydrog. Energy* **2014**, *39*, 21489–21499. [[CrossRef](#)]
- Young, K.; Ng, K.Y.S.; Bendersky, L.A. A Technical Report of the Robust Affordable Next Generation Energy Storage System-BASF program. *Batteries* **2016**, *2*, 2. [[CrossRef](#)]
- Young, K.; Ouchi, T.; Huang, B.; Chao, B.; Fetcenko, M.A.; Bendersky, L.A.; Wang, K.; Chiu, C. The Correlation of C14/C15 Phase Abundance and Electrochemical Properties in the  $AB_2$  Alloys. *J. Alloys Compd.* **2010**, *506*, 841–848. [[CrossRef](#)]
- Young, K.; Nei, J. The Current Status of Hydrogen Storage Alloy Development for Electrochemical Applications. *Materials* **2013**, *6*, 4574–4608. [[CrossRef](#)] [[PubMed](#)]
- Young, K.; Chang, S.; Lin, X. C14 Laves Phase Metal Hydride Alloys for Ni/MH Batteries Applications. *Batteries* **2017**, *3*, 27. [[CrossRef](#)]
- Schlapbach, L.; Seiler, A.; Siegmann, H.C.; Waldkirch, T.V.; Zücher, P.; Brundle, C.R. Self Restoring of the Active Surface in  $LaNi_5$ . *Int. J. Hydrog. Energy* **1979**, *4*, 21–28. [[CrossRef](#)]
- Fetcenko, M.A.; Young, K.; Ovshinsky, S.R.; Reichman, B.; Koch, J.; Mays, W. Modified Electrochemical Hydrogen Storage Alloy Having Increased Capacity, Rate Capability and Catalytic Activity. US Patent 6,740,448, 25 May 2004.
- Meli, F.; Schlapbach, L. Surface Analysis of  $AB_5$ -type electrodes. *J. Less Common Met.* **1991**, *172*, 1252–1259. [[CrossRef](#)]

19. Broom, D.P.; Kemali, M.; Ross, D.K. Magnetic Properties of Commercial Metal Hydride Battery Materials. *J. Alloys Compd.* **1999**, *255*, 293–295. [[CrossRef](#)]
20. Yu, B.; Chen, L.; Wen, M.F.; Tong, M.; Chen, D.M.; Tian, Y.W.; Zhai, Y.C. Surface Modification of AB<sub>2</sub> and AB<sub>5</sub> Hydrogen Storage Alloy Electrodes by the Hot-charging Treatment. *J. Mater. Sci. Technol.* **2001**, *17*, 247–251.
21. Shen, Y.; Peng, F.; Kontos, S.; Noréus, D. Improved NiMH Performance by a Surface Treatment that Creates Magnetic Ni-clusters. *Int. J. Hydrog. Energy* **2016**, *41*, 9933–9938. [[CrossRef](#)]
22. Tan, S.; Shen, Y.; Şahin, E.Q.; Noréus, D.; Öztürk, T. Activation Behavior of an AB<sub>2</sub> Type Metal Hydride Alloy for NiMH Batteries. *Int. J. Hydrog. Energy* **2016**, *41*, 9948–9953. [[CrossRef](#)]
23. Ye, Z.; Noréus, D. Metal hydride electrodes: The Importance of Surface Area. *J. Alloys Compd.* **2016**, *664*, 59–64. [[CrossRef](#)]
24. Young, K.; Chao, B.; Liu, Y.; Nei, J. Microstructures of the Oxides on the Activated AB<sub>2</sub> and AB<sub>5</sub> Metal Hydride Alloys Surface. *J. Alloys Compd.* **2014**, *606*, 97–104. [[CrossRef](#)]
25. Chang, S.; Young, K.; Ouchi, T.; Meng, T.; Nei, J.; Wu, X. Studies on Incorporation of Mg in Zr-based AB<sub>2</sub> Metal Hydride Alloys. *Batteries* **2016**, *2*, 11. [[CrossRef](#)]
26. Young, K.; Wong, D.F.; Nei, J. Effects of Vanadium/nickel Contents in Laves Phase-related Body-centered-cubic Solid Solution Metal Hydride Alloys. *Batteries* **2015**, *1*, 34–53. [[CrossRef](#)]
27. Teraoka, H. Development of Low Self-Discharge Nickel-Metal Hydride Battery. Available online: <http://www.scribd.com/doc/9704685/Teraoka-Article-En> (accessed on 9 April 2016).
28. Kai, T.; Ishida, J.; Yasuoka, S.; Takeno, K. The Effect of Nickel-Metal Hydride Battery's Characteristics with Structure of the Alloy. In Proceedings of the 54th Battery Symposium in Japan, Osaka, Japan, 7–9 October 2013; p. 210.
29. Liu, F.J.; Kitayama, K.; Suda, S. La and Ce-incorporation Effects on the Surface Properties of the Fluorinated (Ti,Xr)(Mn,Cr,Ci)<sub>2</sub> Hydriding Alloys. *Vacuum* **1996**, *47*, 903–906. [[CrossRef](#)]
30. Kim, S.; Lee, J. Activation behaviour of ZrCrNiM<sub>0.05</sub> metal hydride electrode (M = La, Mm (misch metal), Nd). *J. Alloys Compd.* **1992**, *185*, L1–L4. [[CrossRef](#)]
31. Park, H.Y.; Chang, I.; Cho, W.I.; Cho, B.W.; Jang, H.; Lee, S.R.; Yun, K.S. Electrode Characteristics of the Cr and La Doped AB<sub>2</sub>-type Hydrogen Storage Alloys. *Int. J. Hydrog. Energy* **2001**, *26*, 949–955. [[CrossRef](#)]
32. Liu, F.J.; Sandrock, G.; Suda, S. Surface and Metallographic Microstructure of the La-added AB<sub>2</sub> Compound (Ti, Zr)(Mn, Cr, Ni)<sub>2</sub>. *J. Alloys Compd.* **1995**, *231*, 392–396. [[CrossRef](#)]
33. Sun, D.; Latroche, M.; Percheron-Guégan, A. Effects of Lanthanum or Cerium on the Equilibrium of ZrNi<sub>1.2</sub>Mn<sub>0.6</sub>V<sub>0.2</sub>Cr<sub>0.1</sub> and Its Related Hydrogenation Properties. *J. Alloys Compd.* **1997**, *248*, 215–219.
34. Yang, X.G.; Lei, Y.Q.; Shu, K.Y.; Lin, G.F.; Zhang, Q.A.; Zhang, W.K.; Zhang, X.B.; Lu, G.L.; Wang, Q.D. Contribution of Rare-earths to Activation Property of Zr-based Hydride Electrode. *J. Alloys Compd.* **1999**, *293*, 632–636. [[CrossRef](#)]
35. Sun, J.C.; Li, S.; Ji, S.J. The Effects of the Substitution of Ti and La for Zr in ZrMn<sub>0.7</sub>V<sub>0.2</sub>Co<sub>0.1</sub>Ni<sub>1.2</sub> Hydrogen Storage Alloys on the Phase Structure and Electrochemical Properties. *J. Alloys Compd.* **2007**, *446*, 630–634.
36. Chen, W.X. Effects of Addition of Rare-earth Element on Electrochemical Characteristics of ZrNi<sub>1.1</sub>Mn<sub>0.5</sub>V<sub>0.3</sub>Cr<sub>0.1</sub> Hydrogen Storage Alloy Electrodes. *J. Alloys Compd.* **2001**, *319*, 119–123.
37. Young, K.; Ouchi, T.; Huang, B.; Reichman, B.; Fetcenko, M.A. Effect of Molybdenum Content on Structural, Gaseous Storage, and Electrochemical Properties of C14-predominant AB<sub>2</sub> Metal Hydride Alloys. *J. Power Sour.* **2011**, *196*, 8815–8821. [[CrossRef](#)]
38. Young, K.; Nei, J.; Wan, C.; Denys, R.V.; Yartys, V.A. Comparison of C14- and C15-predominated AB<sub>2</sub> Metal Hydride Alloys for Electrochemical Applications. *Batteries* **2017**, *3*, 22. [[CrossRef](#)]
39. Young, K.; Ouchi, T.; Meng, T.; Wong, D.F. Studies on the Synergetic Effects in Multi-phase Metal Hydride Alloys. *Batteries* **2016**, *2*, 15. [[CrossRef](#)]
40. Young, K.; Ouchi, T.; Nei, J.; Koch, J.M.; Lien, Y. Comparison among constituent phases in superlattice metal hydride alloys for battery applications. *Batteries* **2017**. submitted.
41. Koch, J.M.; Young, K.; Nei, J.; Hu, C.; Reichman, B. Performance comparison between AB<sub>5</sub> and superlattice metal hydride alloys in sealed cells. *Batteries* **2017**. submitted.
42. Wang, L.; Young, K.; Meng, T.; Ouchi, T.; Yasuoka, S. Partial Substitution of Cobalt for Nickel in Mixed Rare Earth Metal Based Superlattice Hydrogen Absorbing Alloy—Part 1 Structural, Hydrogen Storage and Electrochemical Properties. *J. Alloys Compd.* **2016**, *660*, 407–415. [[CrossRef](#)]

43. Young, K.; Yasuoka, S. Past, present, and future of metal hydride alloys in nickel-metal hydride batteries. In Proceedings of the 14th International Symposium on Metal-Hydrogen Systems, Manchester, UK, 21–25 July 2014.
44. Zhou, X.; Young, K.; West, J.; Regalado, J.; Cherisol, K. Degradation Mechanisms of High-energy Bipolar Nickel Metal Hydride Battery with AB<sub>5</sub> and A<sub>2</sub>B<sub>7</sub> Alloys. *J. Alloys Compd.* **2013**, *580*, S373–S377. [[CrossRef](#)]
45. Stucki, F.; Schlapbach, L. Magnetic Properties of LaNi<sub>5</sub>, FeTi, Mg<sub>2</sub>Ni and Their Hydrides. *J. Less Common Met.* **1980**, *74*, 143–151. [[CrossRef](#)]
46. Schlapbach, L.; Stucki, F.; Seiler, A.; Siegmann, H.C. Magnetism and Hydrogen Storage in LaNi<sub>5</sub>, FeTi and Mg<sub>2</sub>Ni. *J. Magn. Magn. Mater.* **1980**, *15–18*, 1271–1272. [[CrossRef](#)]
47. Young, K.; Chao, B.; Nei, J. Microstructures of the Activated Si-containing AB<sub>2</sub> Metal Hydride Alloy Surface by Transmission Electron Microscope. *Batteries* **2016**, *2*, 4. [[CrossRef](#)]
48. Young, K.; Chao, B.; Pawlik, D.; Shen, H.T. Transmission Electron Microscope Studies in the Surface Oxide on the La-containing AB<sub>2</sub> Metal Hydride Alloy. *J. Alloys Compd.* **2016**, *672*, 356–365. [[CrossRef](#)]
49. Young, K.H.; Fetcenko, M.A.; Ovshinsky, S.R.; Ouchi, T.; Reichman, B.; Mays, W.C. Improved Surface Catalysis of Zr-based Laves Phase Alloys for NiMH Batteries. In *Hydrogen at Surface and Interfaces*; Jerkiewicz, G., Feliu, J.M., Popov, B.N., Eds.; Electrochemical Society: Pennington, NJ, USA, 2000.
50. Lee, H.; Chourashiya, M.G.; Park, C.; Park, C. Hydrogen Storage and Electrochemical Properties of the Ti<sub>0.32</sub>Cr<sub>0.43–x–y</sub>V<sub>0.25</sub>Fe<sub>x</sub>Mn<sub>y</sub> ( $x = 0–0.055$ ,  $y = 0–0.080$ ) Alloys and Their Composites with MmNi<sub>3.99</sub>Al<sub>0.29</sub>Mn<sub>0.3</sub>Co<sub>0.6</sub> Alloy. *J. Alloys Compd.* **2013**, *566*, 37–42. [[CrossRef](#)]
51. Inoue, H.; Arai, S.; Iwakura, C. Crystallographic and Electrochemical Characterization of TiV<sub>4–x</sub>Ni<sub>x</sub> Alloys for Nickel-metal Hydride Batteries. *Electrochim. Acta* **1996**, *41*, 937–939. [[CrossRef](#)]
52. Yu, X.B.; Wu, Z.; Xia, B.J.; Xu, N.X. A Ti-V-based bcc Phase Alloy for Use as Metal Hydride Electrode with High Discharge Capacity. *J. Chem. Phys.* **2004**, *121*, 987–990. [[CrossRef](#)] [[PubMed](#)]



© 2017 by the authors. Licensee MDPI, Basel, Switzerland. This article is an open access article distributed under the terms and conditions of the Creative Commons Attribution (CC BY) license (<http://creativecommons.org/licenses/by/4.0/>).